Research Square

Preprints are preliminary reports that have not undergone peer review.
They should not be considered conclusive, used to inform clinical practice,
or referenced by the media as validated information.

Tuning Structural, Magnetic, and Photocatalytic Properties of Erbium Orthoferrite Nanoparticles via co-substitution of Gd 3+ and Ti 4+

Anusha Karumuri
Koneru Lakshmaiah Education Foundation
Vani Arja
Koneru Lakshmaiah Education Foundation
Kumara Raja Kandula
Lakireddy Bali Reddy college of Engineering
Tinku Baidya
tinku26@gmail.com

Koneru Lakshmaiah Education Foundation

Research Article

Keywords: ErFeO3, EDTA, Rare earth Orthoferrite, Magnetic properties, Optical properties, Photocatalysis

Posted Date: July 10th, 2026

DOI: https://doi.org/10.21203/rs.3.rs-10079215/v1

License: This work is licensed under a Creative Commons Attribution 4.0 International License.
Read Full License

Additional Declarations: No competing interests reported.

Version of Record: A version of this preprint was published at Applied Physics A on August 27th, 2026.
See the published version at https://doi.org/10.1007/s00339-026-10151-x.

Tuning Structural, Magnetic, and Photocatalytic Properties of Erbium Orthoferrite Nanoparticles via co-substitution of Gd^{3+} and Ti^{4+}

Anusha Karumuri[1, 2] and Arja Vani[2], Kumara Raja kandula[3*], Tinku Baidya[2*†],

[1]Department of Chemistry, Government College for women (A), Guntur-522001, India.
[2]Department of Chemistry, KoneruLakshmaiah Education Foundation, Greenfield, Vaddeswaram, Andhra Pradesh-522502, India.
[3]Devision of Physics, Freshman Engineering Department, Lakireddy Bali Reddy college of Engineering, Mylavaram-521230, India.

Abstract

Erbium Orthoferrite ($ErFeO_3$) nanoparticles are well-known for magnetic and photocatalysis applications, however the crystallite size will play more crucial role to design for particle applications. Scientists were trying to reduce the crystallite size by adopting different synthetic routes or substitution/co- substitution of appropriate atoms or concentration. In these aspects we prepared the $ErFeO_3$ (EFO) nanoparticle by substitution of isovalent ion (Gd^{3+}) at A-site and higher valence ion (Ti^{4+}) at B-site, i.e., $Er_{1-x}Gd_xFe_{1-x}Ti_xO_3$ (where x=0, 2.5, 5 and 7.5 mol%) to tune the chemical and physical properties. The optimized concentration of substitution and co-substitution ion concentration was 5 mol%, which is conformed through X-ray diffraction (XRD) studies convoyed through structure refinement method (Rietveld). The synthesized samples up to 5 mol% was found to be single phase with orthorhombic crystal structure of space group of *Pnma.* space group. The scanning electron microscopy (SEM) was utilized to observe the morphology and also calculate the crystallite size the synthesized materials. BET measurements confirm that the synthesized nanomaterials possess a mesoporous structure, with specific surface areas ranging from 15.978 to 41.465 m^2/g. The X-ray photoelectron spectroscopy (XPS) analysis was carried out to check the Fe oxidation number and to estimate the oxygen vacancy concentration. Nearly two times higher saturation magnetization (M_S) value

was observed for 5 mol% substituted and co- substituted sample when compared to un substituted sample. These results indicate that nanomaterials substituted with 5 mol% Gd and co-substituted with Ti have strong potential for use in gas sensing and photocatalytic applications.

Keywords: $ErFeO_3$, EDTA, Rare earth Orthoferrite, Magnetic properties, Optical properties, Photocatalysis.

Corresponding author: tinkubaidya@kluniversity.in (TB)† & kumar9863@gmail.com (KR) *

1. Introduction

Rare-earth orthoferrites ($RFeO_3$) are a class of perovskite-type oxides that have garnered significant attention due to their remarkable magnetic, optical, and electrical properties [1-5]. Among them, erbium orthoferrite ($ErFeO_3$) stands out as a promising material exhibiting canted antiferromagnetism, weak ferromagnetism, and temperature-induced spin reorientation transitions [6-8]. These characteristics arise primarily from the super-exchange interactions between Fe^{3+} ions mediated by oxygen ions, along with contributions from the rare-earth sublattice. Such materials are considered potential candidates for applications in spintronics, sensors, and multifunctional devices [9-10].

Substitution is an effective strategy to tailor the intrinsic properties of orthoferrites. Substitution at the rare-earth (A-site) with gadolinium (Gd^{3+}) introduces lattice distortions due to ionic radius differences and enhances magnetic interactions owing to Gd's high magnetic moment. This modification can influence the spin reorientation behavior and magnetic ordering temperature. On the other hand, substitution at the Fe-site (B-site) with titanium (Ti^{4+}), a non-magnetic ion, disrupts the Fe–O–Fe exchange pathways, leading to altered magnetic, dielectric, and optical properties. The combined effect of Gd and Ti co- substitution is expected to provide a synergistic tuning of both structural and functional characteristics.

Recent research has demonstrated that co- substitution in orthoferrites can significantly enhance multifunctional properties, including dielectric permittivity, optical absorption, and magnetoelectric coupling [11-12]. However, studies specifically focusing on Gd and Ti co-doped $ErFeO_3$ remain limited. Understanding how dual-site substitution influences structural distortion, exchange interactions, and electronic structure is essential for optimizing these materials for advanced technological applications. Therefore, systematic investigation of Gd and Ti substituted $ErFeO_3$ is crucial to uncover the relationship between composition, structure, and physical properties. Such studies not only contribute to the fundamental understanding of orthoferrite systems but also pave the way for designing materials with tailored properties for next-generation multifunctional devices. Hence, we synthesized Gd and Ti substitution in $ErFeO_3$ using sol-gel route, where EDTA used a chelating agent. The main reason for the use of EDTA as chelating in this invitation was due to smaller particle or crystallite size, abridged lattice strain and improved stability of crystal structure when compared to other chelating agents like urea and acetylacetone [13]. The prepared samples were characterized using different characterization techniques, and explored their magnetic and optical properties.

2. Experimental

2.1 Materials and methods

To prepare the Gd and Ti co- substituted i.e., $Er_{1-x}Gd_xFe_{1-x}Ti_xO_3$ (x= 0, 2.5, 5, 7.5 mol%) nanoparticles, the high purity of raw materials, $Er(NO_3)_3 \cdot 5H_2O$ (99.9%, Sigma-Aldrich), $Fe(NO_3)_3 \cdot 9H_2O$ (99.99%, Merck), $Gd(NO_3)_3 \cdot 5H_2O$ (99.9%, Sigma-Aldrich), $Ti[OCH(CH_3)_2]_4$ (99.5%, Merck) ethylenediaminetetraacetic acid (EDTA, 99.5%, Merck) were used in this investigation. the sol-gel technique was used here. The same procedure, which was reported earlier was used to prepare the $Er_{1-x}Gd_xFe_{1-x}Ti_xO_3$ (x= 0) nanomaterials. However, for x=0.025,

0.05 and 0.075, in acetyl acetone solution the required amount of $Ti[OCH(CH_3)_2]_4$ was mixed [14]. The citric acid solution was added to the above $Ti[OCH(CH_3)_2]_4$ solution and stirred 15 minutes. Then the individual prepared metal nitrates solution, according to stichometry, was added to the above solution with continues stirring. The EDTA solution with 1:2 mol ratio with respect to metal nitrate solution, was slowly added to above solution, and this solution further stirred 30 minutes at room temperature. Then the pH~7 of the above solution was maintained by adding 25% NH_4OH solution with constant stirring, and then entire solution was stirred further 30 minutes. To attain the gel, the pH~7 maintained solution is heated at 80 °C. Then this gel was further heated at 110°C for 3 hours. Then obtained powder was mixed well, and then subjected to calcined at 800°C using muffle furnace with model of Nabertherm L9/11. As a result, we obtained the single nature of Gd and Ti co-doped $ErFeO_3$ nanoparticles.

The crystal structure, phase purity, lattice parameters, crystallite size, and microstrain of the synthesized samples were analyzed by X-ray diffraction (XRD, PANalytical Multifunctional X'Pert) using Cu-Kα radiation (λ = 1.5406 Å) in the 2θ range of 10°–80° with a step size of 0.0167°**.** The surface morphology, particle size, grain distribution, and microstructural features were examined using scanning electron microscopy (SEM, JEOL JSM–IT300LV) operated at an appropriate accelerating voltage. The vibrational characteristics and local structural distortions were investigated by Raman spectroscopy (DXR Raman spectrometer) in the spectral range of 100–1000 cm^{-1}**.** The elemental composition, oxidation states of Fe ions, Fe^{3+}/Fe^{2+} ratio, and oxygen vacancy concentration were determined using X-ray photoelectron spectroscopy (XPS, PHI-5702) with Al Kα radiation (hν = 1486.6 eV)**.** The magnetic properties, including saturation magnetization (M_s), remanent magnetization (M_r), and coercivity (Hc), were measured at room temperature using a vibrating sample magnetometer (VSM, EZ9, MicroSense, USA) under an

applied magnetic field of up to ±20 kOe**.** Furthermore, the specific surface area and pore characteristics were evaluated by N_2 adsorption–desorption measurements using the Brunauer–Emmett–Teller (BET) method **on a** Quantachrome Instruments analyzer (v11.05) after degassing the samples to remove physically adsorbed species. These characterization techniques collectively provided detailed insights into the structural, microstructural, surface, chemical, and magnetic properties of the synthesized materials.

3. Results and Discussion

Partial co- substitution of Gd and Ti ions into the $ErFeO_3$ lattice are expected to influence the XRD peak positions, leading to either shifts toward higher or lower diffraction angles due to differences in ionic radii. To examine this effect, room-temperature XRD patterns of $Er_{1-x}Gd_xFe_{1-x}Ti_xO_3$ (x= 0, 2.5, 5, 7.5 mol%) samples were recorded and are presented in Fig. 1. The observed diffraction peaks were compared with standard data corresponding to an orthorhombic structure with the *Pnma* space group (JCPDS No. 86-0171) [15], which is also included in the figure for reference. The analysis confirms that all samples except 7.5 mol% retain a single-phase orthorhombic structure without any detectable impurity peaks, indicating that the synthesis process was effective and yielded phase-pure compounds. However, the 7.5 mol% Gd and Ti co-substitution $ErFeO_3$ shows the unreacted Er_2O_3 peak, which suggest that the maximum 5 mol% of Gd and Ti ions are incorporating in $ErFeO_3$ crystal lattice. Hence, the 7.5 mol% Gd and Ti co-substitution $ErFeO_3$ not considered for further analysis due to impurity phase. A clear shift of the main diffraction peaks toward lower 2θ values is observed upon the incorporation of Gd^{3+} and Ti^{4+} ions, as highlighted in the magnified view of the most intense peak in **Fig. 1**. This shift is primarily associated with lattice expansion caused by ionic size mismatch between the host and dopant ions. Specifically, the ionic radius of Er^{3+} (1.004 Å, 8-fold coordination) is smaller than

that of Gd^{3+} (1.053 Å), and replacing Er^{3+} with Gd^{3+} introduces lattice strain that increases the interplanar spacing. According to Bragg's law ($n\lambda = 2d \sin\theta$), this increase in spacing results in a shift of diffraction peaks toward lower angles. In contrast, substitution at the Fe-site involves replacing Fe^{3+} ions (0.645 Å, 6-xfold coordination) with slightly smaller Ti^{4+} ions (0.605 Å). While this substitution tends to reduce the local lattice dimensions, its overall impact is comparatively minor. The dominant structural effect arises from the larger Gd^{3+} ions at the A-site, leading to a net expansion of the crystal lattice. Furthermore, the absence of any additional or unidentified peaks in the XRD patterns confirms that Gd^{3+} and Ti^{4+} ions are successfully incorporated into their respective lattice sites, rather than forming secondary phases or segregated impurities.

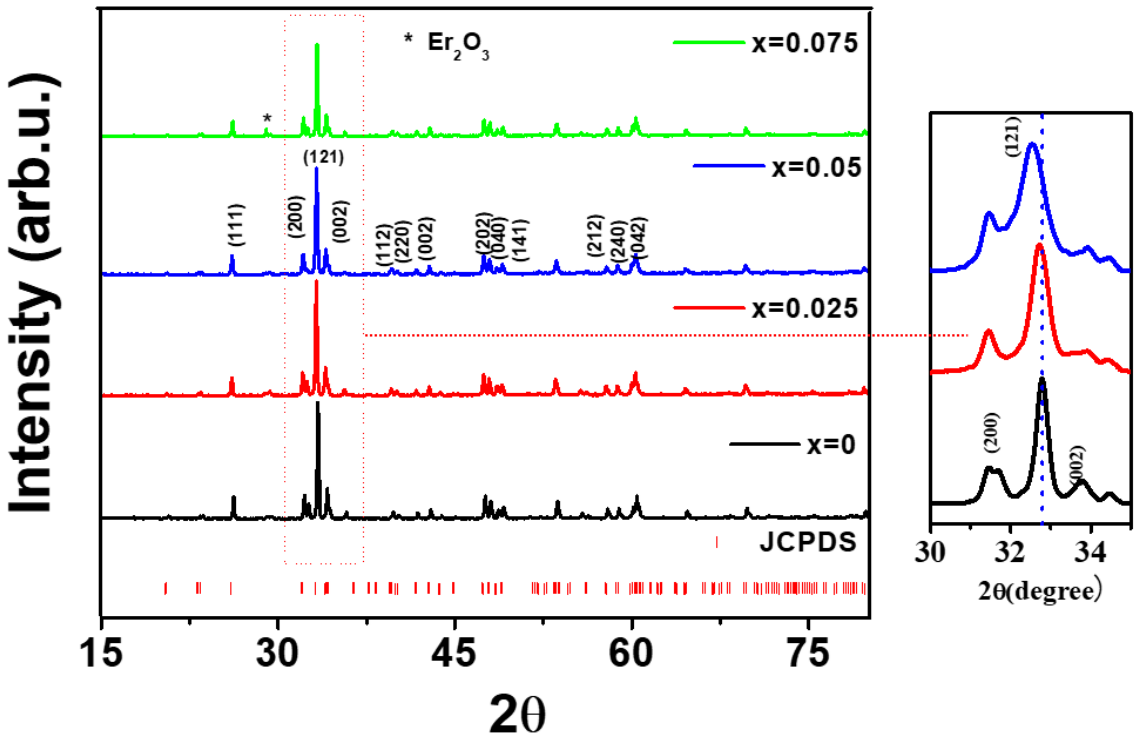
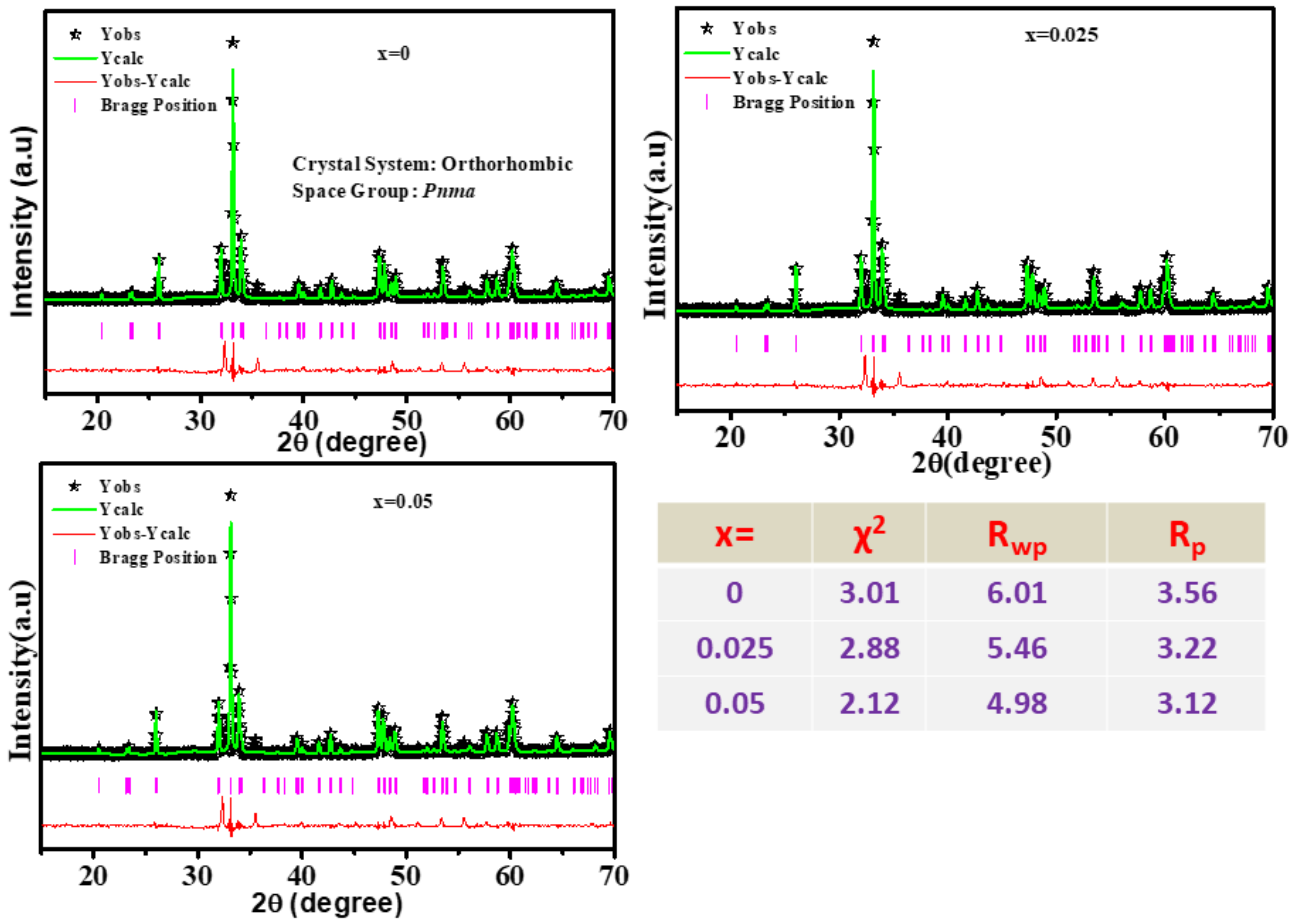


Figure 1: 2θ range of 15º–80º of XRD patterns for $Er_{1-x}Gd_xFe_{1-x}Ti_xO_3$ nanomaterials obtained at room temperature, right side shows the enlarged view of 2θ from 30º to 34.5º

The Rietveld-refined XRD patterns of $Er_{1-x}Gd_xFe_{1-x}Ti_xO_3$ (x= 0, 2.5, 5 mol%) samples are presented in Fig. 2. The analysis confirms that the entire sample adopts an orthorhombic crystal structure with the *Pnma* space group (JCPDS No. 86-0171). **Fig. 3** illustrates the variation in Fe–O–Fe bond angles (Fe–O_1–Fe and Fe–O_2–Fe) along with changes in unit cell volume for all the samples (pure phase sample). The results show that Gd substitution leads to an increase in lattice volume, which can be attributed to the larger ionic radius of Gd^{3+} compared to Er^{3+}. This size mismatch induces lattice expansion, reflected in the experimentally observed increase in unit cell parameters. Moreover, the calculated lattice parameters of each sample are provided in table 2. In addition to this, we also calculated the crystallite size of each sample (pure phase) using Williamson-Hall (W-H) plot, and thus obtained W-H plots and size of each material was mentioned in **Fig 4**. The decreased crystallite size with increase of Gd and Ti co- substitution in $ErFeO_3$ is mainly due to strain, defects, and grain boundary pinning.



x=	χ^2	R_{wp}	R_p
0	3.01	6.01	3.56
0.025	2.88	5.46	3.22
0.05	2.12	4.98	3.12

Figure 2: Refinement (Rietveld) XRD graphs of $Er_{1-x}Gd_xFe_{1-x}Ti_xO_3$ (x= 0, 2.5, 5 mol%) nanomaterials and its refinement parameters.

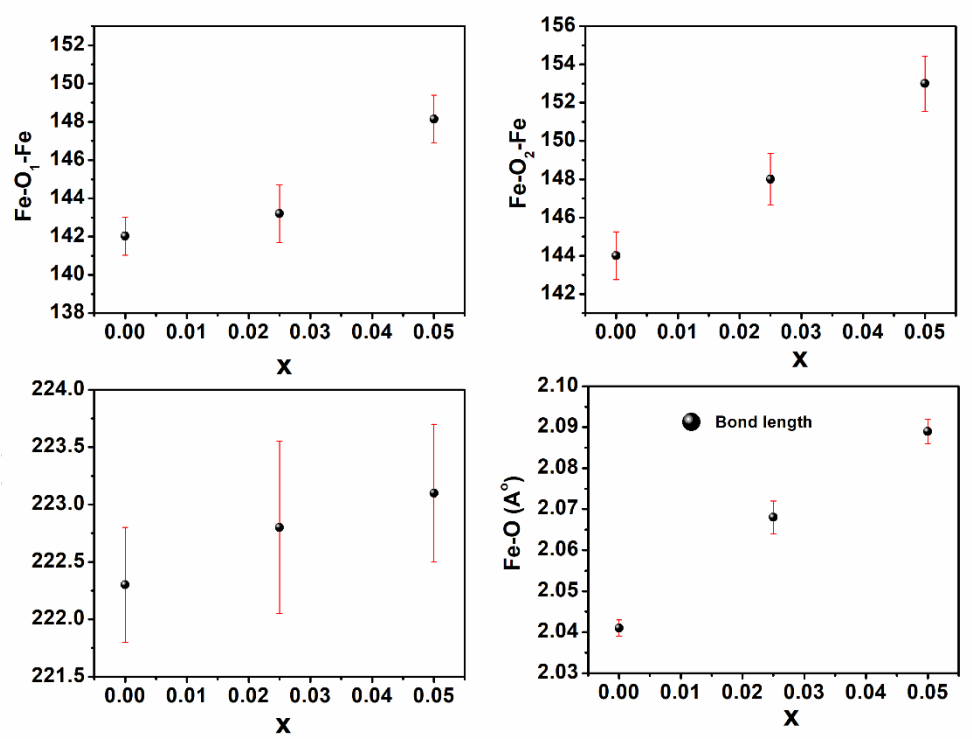


Figure 3: Bong angle, cell volume and bond length of $Er_{1-x}Gd_xFe_{1-x}Ti_xO_3$ nanomaterials

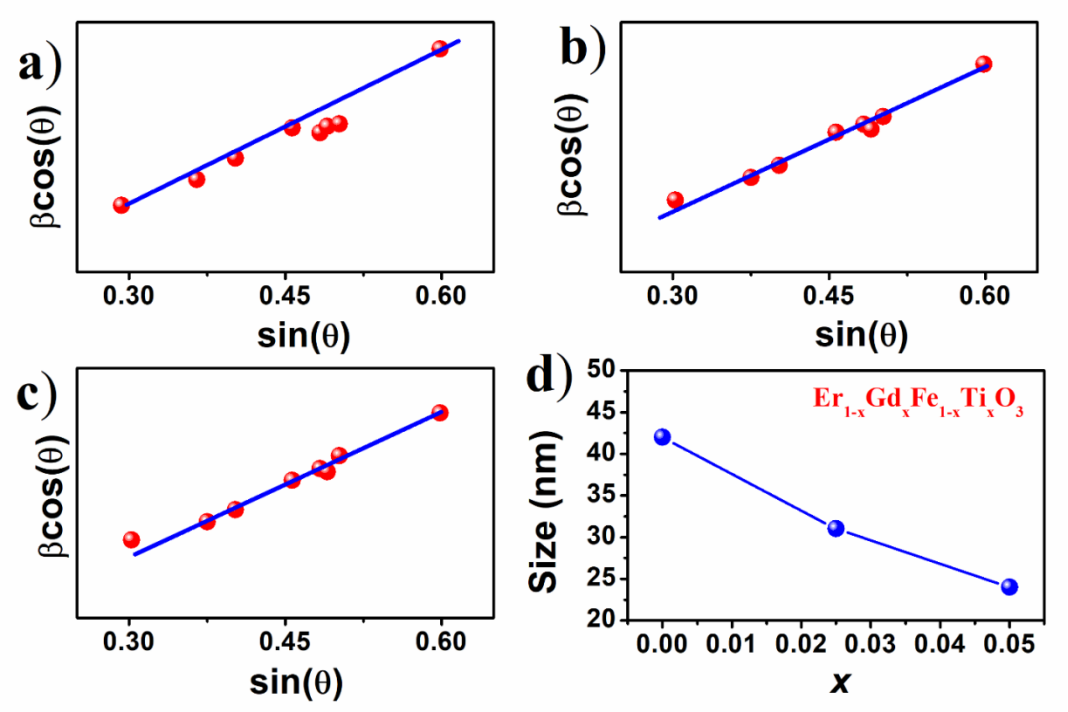


Figure 4: W–H plots for $Er_{1-x}Gd_xFe_{1-x}Ti_xO_3$ nanomaterials; x=0 (a), x=0.025 (b), x=0.05 (c) and d) crystallite size

Table 2: Lattice parameters, Fe-O-Fe bond angle (θ_1, θ_2), Fe-O bond length, tilt angles, D, strain, Refinement parameters of $Er_{1-x}Gd_xFe_{1-x}Ti_xO_3$ (x= 0, 2.5, 5 mol%) nanomaterials

Lattice Parameters	**$Er_{1-x}Gd_xFe_{1-x}Ti_xO_3$**		
	x=0	x=0.025	x=0.05
a (Å)	5.2649 (3)	5.2653 (3)	5.2659 (3)
b(Å)	7.4348 (2)	7.4351 (3)	7.4356 (3)
c(Å)	5.2412 (4)	5.2414 (4)	5.2418 (4)
α=β=γ=90°C			

The effects of Gd^{3+} substitution and Ti^{4+} co- substitution on the $ErFeO_3$ matrix were investigated using Raman spectroscopy at room temperature (RT) to gain deeper insight into the structural modifications. The Raman spectra of $Er_{1-x}Gd_xFe_{1-x}Ti_xO_3$ nanomaterials recorded in the range of 50–750 cm^{-1} are presented in **Fig. 5**. Based on group theoretical analysis [16], rare-earth orthoferrites exhibit the following irreducible representation at the Γ ($7A_{1g}+7B_{1g}+5B_{2g}+5B_{3g}+8A_{1u}+10B_{2u}+10B_{3u}+8B_{1u}$). Among these, the $8A_1u$ modes are optically inactive, while 24 modes ($7A_1g + 7B_1g + 5B_2g + 5B_3g$) are Raman-active and 28 modes ($10B_2u + 10B_3u + 8B_1u$) are infrared-active [17]. In the present study, 12 Raman-active modes were clearly observed at room temperature for $Er_{1-x}Gd_xFe_{1-x}Ti_xO_3$ nanomaterials. These include two B_1g modes (~153.8 and 326.1 cm^{-1}), one B_2g mode (~477.4 cm^{-1}), two B_3g modes (~252.9 and 374.7 cm^{-1}), and seven A_1g modes located at approximately 103.4, 133.2, 272.6, 334.5, 413.9, 440.3, and 495.7 cm^{-1}. The observed vibrational modes are consistent with previously reported results for orthoferrite systems. A noticeable change in peak characteristics was observed upon substitution and co- substitution. The relatively broad Raman bands of unsubstituted $ErFeO_3$ (x=0) become sharper after Gd^{3+} and Ti^{4+} incorporation, indicating modifications in structural order and local lattice environment. The low-frequency modes around 103.4, 133.2, and 153.8

cm^{-1} are particularly sensitive to substitution, showing shifts toward higher wavenumbers, which can be attributed to ionic radius mismatch and induced lattice distortion. In contrast, the higher-frequency modes such as 413.9, 440.3, and 495.7 cm^{-1} are associated mainly with oxygen vibrations, exhibit slight shifts toward lower wavenumbers. This behaviour may be related to changes in bond strength and local structural rearrangements caused by increasing dopant concentration. These Raman results are in good agreement with the structural trends observed from X-ray diffraction analysis.

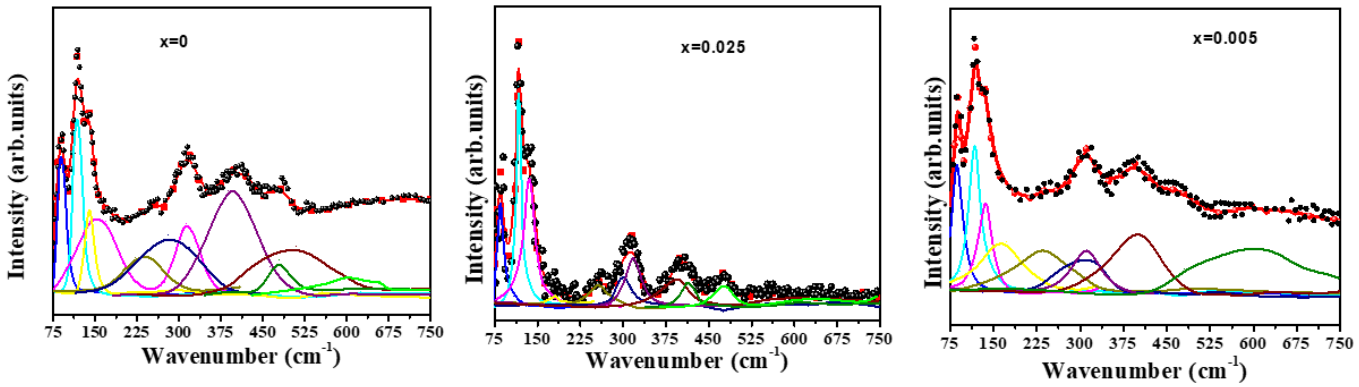


Figure 5: Raman spectra of $Er_{1-x}Gd_xFe_{1-x}Ti_x$ $Er_{1-x}Gd_xFe_{1-x}Ti_xO_3$ (x= 0, 2.5, 5 mol%)O_3 nanomaterials

Generally, in ferrite systems, the introduction of higher-valence dopant ions such as Ti^{4+} into the Fe^{3+} sublattice significantly influences the oxygen stoichiometry through charge compensation mechanisms. When Ti^{4+} substitutes for Fe^{3+}, an excess positive charge is introduced into the lattice, which must be balanced to maintain overall electrical neutrality. Although this imbalance is often compensated by the formation of oxygen vacancies, an alternative and energetically favourable mechanism involves the partial reduction of Fe^{3+} to Fe^{2+} [18]. At higher substitution concentrations, this valence adjustment becomes more dominant, thereby reducing the necessity for additional oxygen vacancy formation. Furthermore, in materials that initially possess a

considerable concentration of intrinsic oxygen vacancies, the incorporation of higher-valence ions can lead to their annihilation or stabilization, effectively improving oxygen stoichiometry. As a result, despite the introduction of aliovalent dopants, the overall oxygen vacancy concentration may decrease with increasing dopant content. This behaviour highlights the complex interplay between defect chemistry, charge compensation, and lattice stability in substituted ferrite materials.

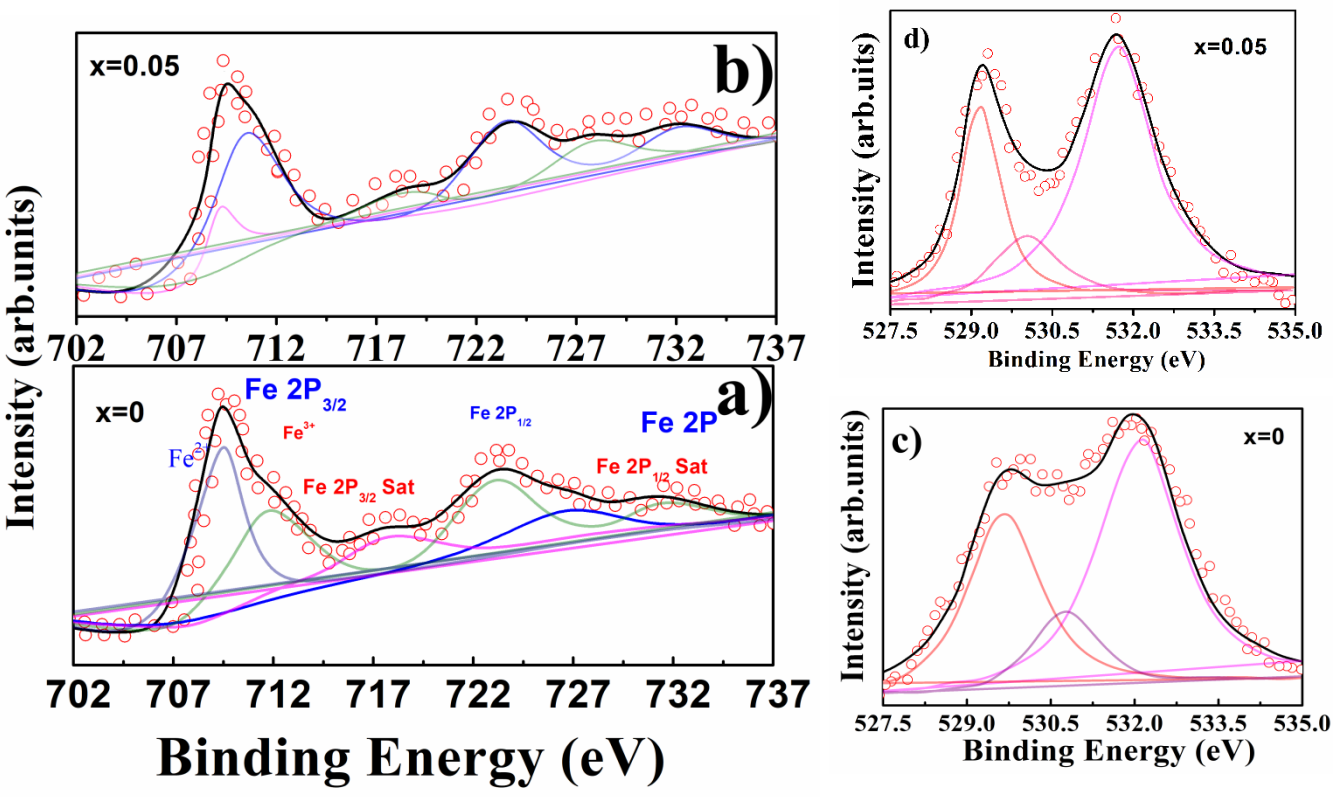


Figure 6: XPS analysis of Fe atom a) *x*=0 and b) *x*=0. 05, and oxygen atom c) *x*=0 and d) *x*=0.05 samples.

To further understand the oxygen vacancy concentration and Fe^{3+}/Fe^{2+}, XPS analysis was performed for two samples (*x*=0 and *x*=0.05), and thus obtained graphs as shown in **Fig. 6**. The Fe 2p spectrum exhibits characteristic peaks corresponding to Fe $2p_{3/2}$ and Fe $2p_{1/2}$, confirming

the presence of Fe–O bonding within the material [19]. Deconvolution of these peaks enabled estimation of the relative amounts of Fe^{3+} and Fe^{2+} species. The calculated Fe^{2+}: Fe^{3+} ratios were 52.18 for x = 0 and 24.18 for x = 0.05, indicating that incorporation of high valency (Ti^{4+}) atom at Fe^{3+} site into the $ErFeO_3$ matrix suppresses the reduction of Fe^{3+} to Fe^{2+}. In addition, the concentration of oxygen vacancies was evaluated from the O 1s XPS spectra. The estimated vacancy concentrations were 31.27 for the x=0 sample (Fig 6 (c)) and 21.83 for the x=0.05 sample (Fig 6 (c)), suggesting a decrease in oxygen deficiency upon high valency (Ti^{4+}) atom at Fe^{3+} site into the $ErFeO_3$ matrix.

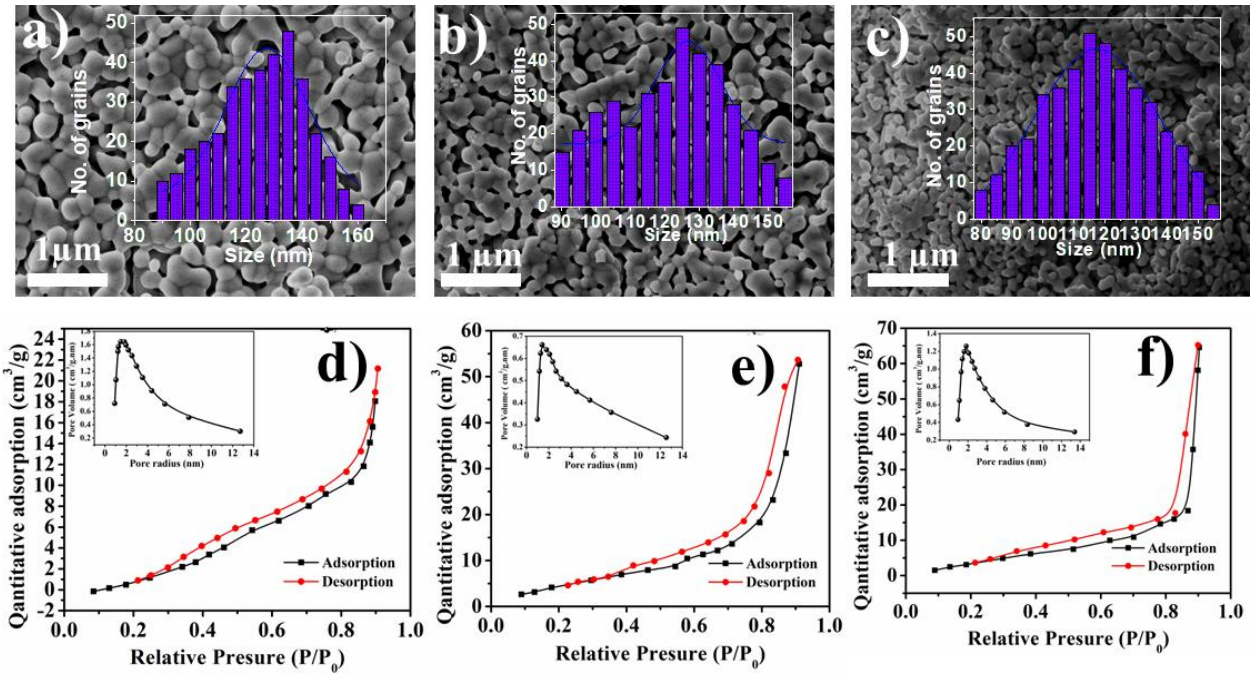


Figure 7: SEM analysis of $Er_{1-x}Gd_xFe_{1-x}Ti_xO_3$ nanomaterials, a) x=0, b) x=0.025 and c) x=0.05, and insert shows the histogram crystallite size and BET analysis d) x=0, e) x=0.025 and f) x=0.05, and insert shows average pore size

To find the average grain size and morphology of the $Er_{1-x}Gd_xFe_{1-x}Ti_xO_3$ nanomaterials, SEM examination was achieved and thus attained images were depicted in Fig.7. The synthesized samples (pure phase) exhibit comparable morphological features, although a

noticeable difference in grain size is observed. The average grain size of the un substitution sample (x = 0) is approximately 138 nm, whereas it decreases to 115 nm for the substituted composition (x = 0.05). This reduction in grain size can be attributed to the mismatch between the ionic radii of the dopant ions and those of the host lattice. Such mismatch promotes the migration and segregation of dopant ions toward grain boundaries during the sintering process. The presence of these segregated ions impedes grain boundary mobility, thereby suppressing grain growth [20]. Additionally, this segregation induces lattice strain and structural distortion, which further contributes to the refinement of grains by facilitating the nucleation of new crystallites.

The surface characteristics of the $Er_{1-x}Gd_xFe_{1-x}Ti_xO_3$ nanomaterials were investigated using the Brunauer–Emmett–Teller (BET) technique. The nitrogen adsorption–desorption isotherms, shown in **Fig. 7 (d–f)**, exhibit type IV behaviour, which is characteristic of mesoporous materials. The pore size distribution, surface area, and porosity were determined using the Barrett–Joyner–Halenda (BJH) method, and the corresponding plots are presented as insets in **Fig. 7 (d–f)**. These results confirm the porous nature of all samples. The measured specific surface areas are 15.978, 34.871, 41.465 m^2/g for x=0, 0.025 and 0.05, respectively. The average pore diameters are found to be 3.49, 3.42 and 3.39, for the corresponding compositions. These pore size values fall within the mesoporous range, indicating that all synthesized materials possess mesoporous structures. It is also observed that the specific surface area increases with increasing Gd and Ti concentration in $ErFeO_3$ matrix. Such features, including high surface area, controlled porosity, and reduced particle size, play a crucial role in enhancing photocatalytic activity or gas sensing performance by providing more active sites for gas adsorption and improving surface reactivity.

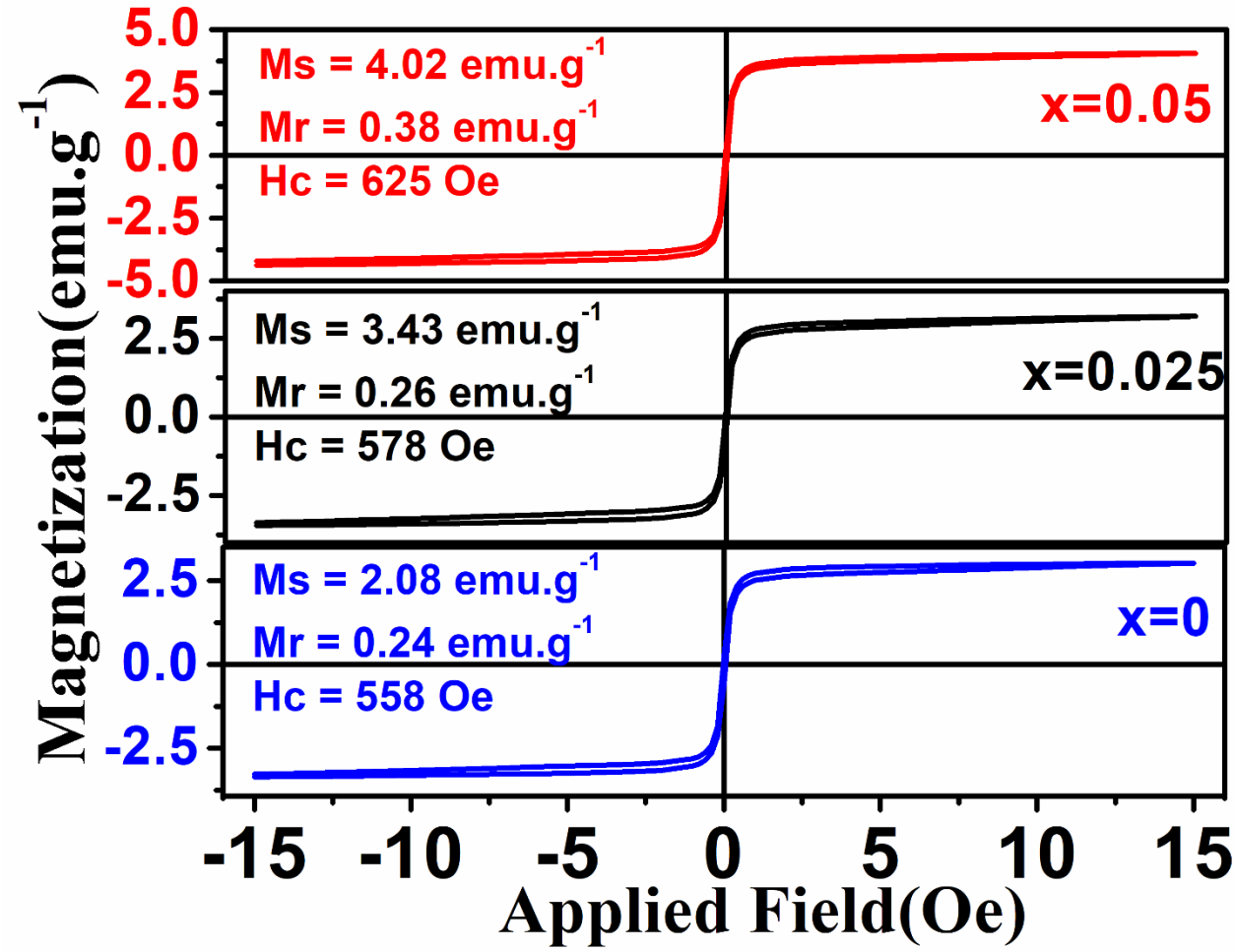


Figure 8: M-H loops of $Er_{1-x}Gd_xFe_{1-x}Ti_xO_3$ (x= 0, 2.5, 5 mol%) nanomaterials.

The magnetic characteristics of orthoferrite compounds are primarily governed by their spin arrangement and magnetic symmetry. In most cases, the rare-earth (R^{3+}) ions are diamagnetic and possess negligible magnetic moments, thus contributing minimally to the overall magnetization. Instead, the magnetic behavior is dominated by Fe^{3+} ions, which carry significant magnetic moments due to the presence of unpaired electrons. The collective alignment and interaction of these Fe^{3+} spins determine the net magnetic properties of the material. In the orthorhombic crystal structure of orthoferrite, each Fe^{3+} ion is surrounded by six O^{2-} ions, forming FeO_6 octahedra [21]. Magnetic coupling between adjacent Fe ions occurs through Fe–

O–Fe super-exchange interactions, where neighboring octahedra share oxygen atoms at their corners. Despite the presence of magnetic Fe^{3+} ions, the overall magnetic moment ideally cancels out because the Fe^{3+}sublattices are aligned antiparallel, resulting in antiferromagnetic ordering. The magnetic hysteresis loops of $Er_{1-x}Gd_xFe_{1-x}Ti_xO_3$ (x= 0, 2.5, 5 mol%) samples (Fig. 8) exhibit unsaturated magnetization, confirming their antiferromagnetic nature. The remanent magnetization (M_r), maximum magnetization (M_m), and coercivity (Hc) increase as Gd and Ti ion concentration rises from 0 to 0.05, as summarized in their respective graphs (**Fig. 8**). Although Gd^{3+} and Ti^{4+} ions are inherently paramagnetic, an enhancement in magnetization is observed with increasing dopant concentration in the $ErFeO_3$ perovskite system. These magnetic parameters are influenced by both intrinsic factors such as cation distribution and substitution and co-substitution ion concentration, chemical composition and extrinsic factors, including microstructure and sample density. Previous studies have shown that magnetic properties correlate strongly with structural parameters: they tend to increase with larger Fe–O–Fe bond angles and R–O bond lengths, while decreasing with shorter Fe–O bond lengths and reduced FeO_6 octahedral volume. In the present case, the enhanced magnetization observed for the x=0.05 sample can be attributed to increased bond angles and R–O distances, which strengthen Er–Fe interactions while weakening Fe–Fe coupling. The weak ferromagnetic behavior observed in these materials can be explained by the Dzyaloshinskii–Moriya (DM) interaction, an antisymmetric exchange mechanism that induces slight canting of spins in distorted crystal structures. As a result, the magnetic moments of Fe^{3+} ions are not perfectly antiparallel, leading to a small but finite net magnetization.

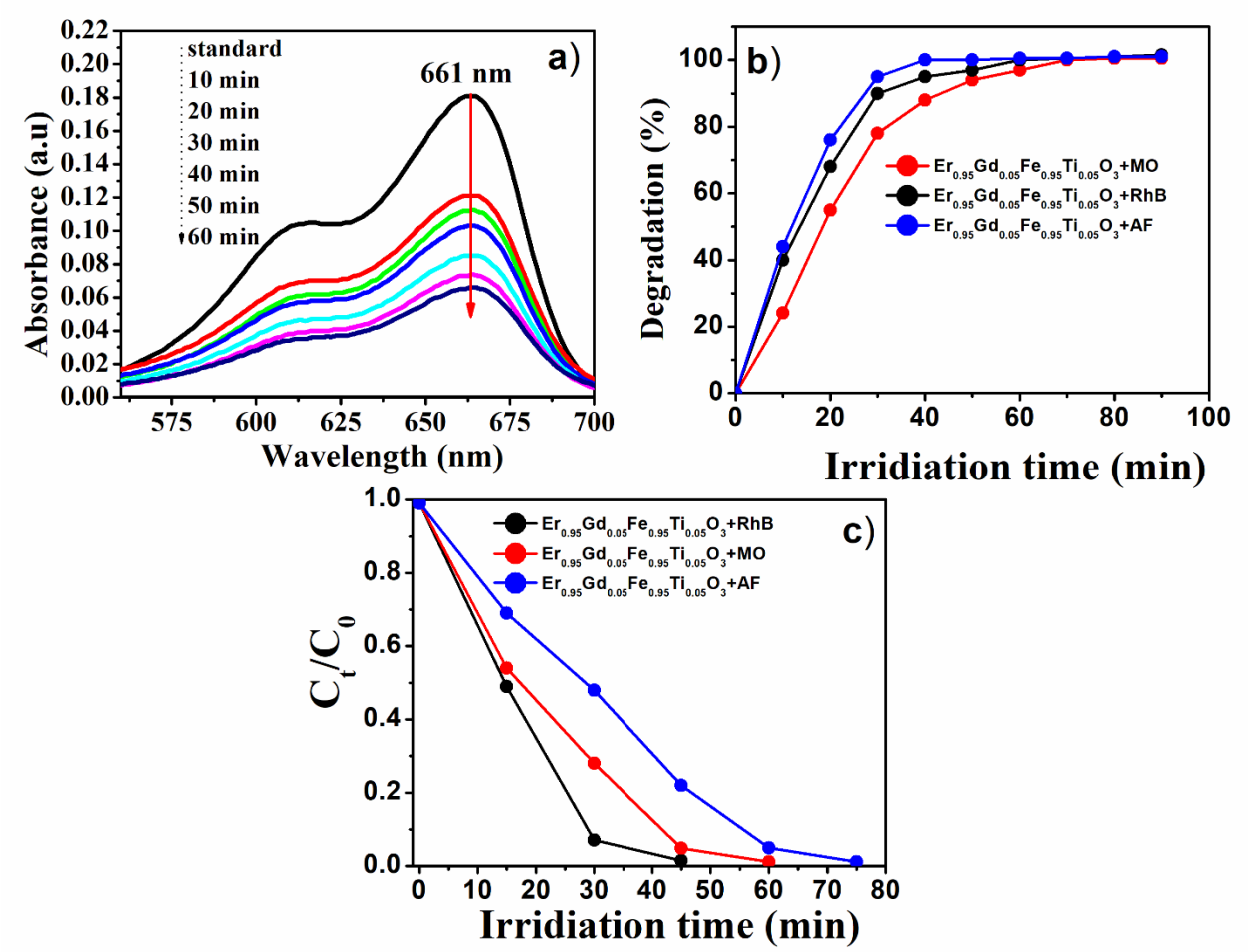


Figure 9: (a) Absorption vs wavelength, (b) % of degradation efficiency and (c) Irradiation time vs C_t/C_0 $Er_{1-x}Gd_xFe_{1-x}Ti_xO_3$ (x= 5 mol%) nanomaterials with different organic dyes.

Finally, the efficiency of photocatalytic degradation was also tested under visible light for 3 organic dyes such as Rhodamine B (RhB), Methyl Orange (MO) and Acid Fuchsin (AF). The degradation efficiency of these three organic dyes was studied and reported in our earlier studies. The wavelength vs absorption plots of different irradiation time with different dye solution with catalysis were recorded using the Uv-Vis instruments, which was mentioned in **Fig 9 (a).** Using these plots the rate constant and % of degradation efficiency was calculated from **Fig 9 (b)** and 9(c). The reported rate constants (k) for MO, RhB and AF were of 0.0314, 0.0457 and 0.0382 min^{-1}, respectively, and corresponding their efficiencies were ~88%, ~94%, and ~91%. To

evaluate the degradation efficiency and rate constant of $Er_{1-x}Gd_xFe_{1-x}Ti_xO_3$ (x=0.05) samples, the procedure was adopted here. The observed rata constant was 0.042 min^{-1} for AF, 0.053 min^{-1} for RhB and 0.086 min^{-1} for MO, however their corresponding % of degradation efficiency was ~94 %, ~96% and ~90%, respectively. The improved rate constant and % of degradation efficiency is mainly due to the enhanced surface area, which was observed in **Fig. 7**

4. Conclusions

Here $ErFeO_3$, $Er_{0.975}Gd_{0.025}Fe_{0.975}Ti_{0.025}O_3$, $Er_{0.95}Gd_{0.02}Fe_{0.95}Ti_{0.05}O_3$ and $Er_{0.925}$ $Gd_{0.075}$ $Fe_{0.925}$ $Ti_{0.075}O_3$ nanomaterials were prepared through sol-gel method. $ErFeO_3$, $Er_{0.975}$ $Gd_{0.025}$ $Fe_{0.975}$ $Ti_{0.025}O_3$ and $Er_{0.95}Gd_{0.02}Fe_{0.95}Ti_{0.05}O_3$ nanomaterials shows the pure/single phase which was conformed through XRD analysis and Rietveld refinement. Due to miss match of ionic radii between substituted ions and host matrix ions, the bond length and bond angle changes were noticed. The reduction of average size was through SEM analysis, with an increase of Gd and Ti concentration in host matrix. These samples shows the mesoporous nature, and the surface area increases from 15.978 to 41.465 m^2/g with an increase of Gd and Ti concentration from 0 to 0.05 mol in host matrix. XPS analysis confirmed the coexistence of Fe^{3+} and Fe^{2+}states, with Fe^{3+}/Fe^{2+} ratios of 52.18 for $ErFeO_3$ and 24.18 for $Er_{0.95}Gd_{0.02}Fe_{0.95}Ti_{0.05}O_3$, while the corresponding oxygen vacancy concentrations were 31.27 and 21.83, respectively. The *Ms* values 2.08 emu/g for $ErFeO_3$ 3.12 and 4.02 emu/g for $Er_{0.95}Gd_{0.02}Fe_{0.95}Ti_{0.05}O_3$, while the corresponding coercive field (Oe) were 558 and 625 Oe respectively. In conclusion the higher surface area, improved magnetization value and improved degradation efficiency and rate constant, the $Er_{0.95}Gd_{0.02}Fe_{0.95}Ti_{0.05}O_3$ nanoparticles could be probable candidates for applications of gas sensing and photocatalysis.

ACKNOWLEDGMENTS:

The authors Dr. Tinku Baidya gratefully acknowledge the Department of Chemistry, Koneru Lakshmaiah Education Foundation, India, for providing the experimental facilities and instrumental support required to carry out this research work.

Data Availability

The authors declare that all the data generated or analyzed during this study are included in this manuscript

Conflict of Interest

The authors declare that they have no conflict of interest.

Funding Declaration: The authors declare that no specific funding was received from any funding agency in the public, commercial, or not-for-profit sectors for the research, authorship, and/or publication of this article.

CRediT authorship contribution statement:

Anusha Karumuri: contributed to methodology, investigation, data curation, formal analysis, visualization, and prepared the original draft of the manuscript. **Arja Vani:** contributed to methodology and investigation. **Kumara Raja Kandula:** contributed to conceptualization, formal analysis, and supervision. **Tinku Baidya:** contributed to conceptualization, supervision, project administration, resources, funding acquisition, and manuscript review and editing. All authors reviewed and approved the final version of the manuscript.

References

1. M. Chouhan, H. Chouhan, D. Basumatary, R. K. Parida, B. N. Parida, Recent advances in rare-earth orthoferrites: Synthesis, dielectric-magnetic properties, and multifunctional applications, ***Ceram. Int.*** (2026).
2. Z. Q. Wang, Y. S. Lan, Z. Y. Zeng, X. R. Chen, Q. F. Chen, Magnetic structures and optical properties of rare-earth orthoferrites $RFeO_3$ (R = Ho, Er, Tm and Lu), ***Solid State Commun.***, 288, 10–17 (2019).
3. X. Chen, Z. Hua, C. Geng, N. Ma, Facile synthesis of novel $YbFeO_3$–$BiFeO_3$ composite for highly sensitive ppb-level acetone sensing at low temperature, ***J. Mater. Sci.: Mater. Electron.***, 34, 1588 (2023).
4. V. V. Menshenin, A. P. Nosov, Electro-optic effect in hexagonal compounds $RFeO_3$, ***Phys. Met. Metallogr.***, 125, 579–583 (2024).
5. P. Kumari, V. Srivastava, R. Sharma, H. Ullah, Exploration of optoelectronic, thermodynamic, and thermoelectric properties of $RFeO_3$ (R = Pr, Nd) perovskites, ***Mater. Sci. Eng. B***, 299, 117044 (2024).
6. V. Krishna, R. M. Sarguna, K. Ganesan, R. Ramaseshan, C. Kamal, S. Ganesamoorthy, Structural, dielectric, and mechanical properties of $ErFeO_3$ single crystal grown using optical floating zone method, ***Appl. Phys. A***, 131, 995 (2025).
7. D. G. Oh, J. H. Kim, H. J. Shin, Y. J. Choi, N. Lee, Anisotropic and nonlinear magnetodielectric effects in orthoferrite $ErFeO_3$ single crystals, ***Sci. Rep.***, 10(1), 11825 (2020).
8. M. Alam, K. Mandal, Origin of ferroelectricity in multiferroic $ErFeO_3$, ***Phys. B: Condens. Matter***, 612, 412935 (2021).

9. H. Shen, P. Feng, G. Jiang, Q. Xian, Synthesis of Mn-doped $ErFeO_3$ with enhanced photo and vibration catalytic activities, ***J. Sol-Gel Sci. Technol.***, 95(1), 230–238 (2020).

10. M. K. Warshi, V. Mishra, A. Sagdeo, V. Mishra, R. Kumar, P. R. Sagdeo, Structural, optical and electronic properties of $RFeO_3$, ***Ceram. Int.***, 44(7), 8344–8349 (2018).

11. S. Sharma, S. Khan, Tailoring the structural, optical, electrical and multiferroic properties of $Sm_{1-x}R_xFeO_3$ and their photocatalytic activity, ***Ceram. Int.***, 50(6), 9185–9205 (2024).

12. P. S. J. Bharadwaj, S. Kundu, V. S. Kollipar, K. B. R. Varma, Synergistic effect of co-doping on antiferromagnetic $YFeO_3$, ***RSC Adv.***, 10, 22183–22195 (2020).

13. A. M. Hashem et al., EDTA as chelating agent for sol-gel synthesis of spinel $LiMn_2O_4$ cathode material, ***J. Alloys Compd.***, 737, 758–766 (2018).

14. S. Tukaram, R. Bhimireddi, K. B. R. Varma, Nano/micro $Sr_2Bi_4Ti_5O_{18}$ crystallites: Size dependent properties, ***Mater. Sci. Eng. B***, 211, 101–109 (2016).

15. S. Sharma, N. Ahmad, S. Khan, Effect on structural and magnetic properties of co-doped $SmFeO_3$ nanostructures, ***J. Mater. Sci.: Mater. Electron.***, 34(6), 476 (2023).

16. M. C. Weber et al., Raman spectroscopy of rare-earth orthoferrites $RFeO_3$, ***Phys. Rev. B***, 94, 214103 (2016).

17. A. Q. Wang et al., Preparation and gas sensing properties of $EuFeO_3$ nanofibers, ***Vacuum***, 115414 (2026).

18. Q. Yu et al., Unveiling iron doping activation in lithium-rich cathode, ***J. Mater. Sci.***, 61(5), 3158–3170 (2026).

19. C. Purnawan et al., Influence of Fe^{2+} and Fe^{3+} on TiO_2 properties, ***Trends Sci.***, 23(6), 12406 (2026).

20. B. Yadav et al., Grain boundary diffusion in complex alloys: A review, ***Int. Mater. Rev.***, 71(2), 129–177 (2026).

21. H. Du et al., Investigation of Fe valence evolution in $NdFeO_3$, ***Mod. Phys. Lett. B*** (2026).